



# An adaptive matrix material extrusion optimization model for in situ impregnated continuous fiber-reinforced 3D printing

Jinxiu Yang<sup>1</sup> · Yingxin Ma<sup>1</sup> · Ling Chen<sup>2</sup> · Lijing Zhang<sup>2</sup> · Huanxiao Wu<sup>1</sup> · Yuan Yao<sup>3,4</sup>

Received: 14 March 2023 / Accepted: 29 August 2023 / Published online: 3 October 2023  
© The Author(s), under exclusive licence to Springer-Verlag London Ltd., part of Springer Nature 2023

## Abstract

Microscopic porosity is an important cause of structural failure in 3D printing of continuous fiber reinforced polymer. To reduce the overfilling and underfilling caused during the fabrication of the molten filament under a continuous path and avoid microscopic porosity, this study proposes an adaptive co-extrusion control and optimization model to achieve uniform filling of the matrix material by dynamic adjustment. This optimization process first models the mixture ratio of the matrix material and reinforcing material using an online prepreg co-extrusion fiber filament fabrication process and then constructs a dynamic adjustment factor by analyzing the geometry of the deposition path. The dynamic extrusion volume adjustment model takes the tool path and outputs the optimized process code; therefore, it can be adapted as a post-process for similar 3D printing slicing and path planning procedures. Compared with the co-extruded model that is not optimized for matrix adaptive adjustment, the tensile and flexural strengths increased by 18% and 23.4%, respectively. The porosity decreased by 54.4%. In particular, structural failure owing to uneven filling of fiber-reinforced printed parts is avoided.

**Keywords** 3D printing · Continuous fiber · Deposition spacing · Dynamic extrusion

## 1 Introduction

The continuous fiber reinforced polymer composites (CFRTC) have the advantages of high strength, high modulus, lightweight, high thermal stability, designability, etc. [1–3], which has been widely used in automotive, electronics, aerospace, medical, and in other industries. CFRTC-based fused filament fabrication (FFF) printing can provide better strength and stiffness while guaranteeing structures with customized shapes and fiber orientations and has become a vital method to improve the performance of 3D printing.

There are two main methods for realizing a CFRTC-based FFF process. The first method uses a prepreg continuous fiber as the feed filament. The prepreg filament is fed into the high-temperature print head and extruded directly into the stack according to the FFF process for building composite structures [4–6]. This method enables the secondary impregnation of fibers and matrix during the printing process, improving

impregnation effect, and reduction in porosity. However, this method requires specific dies and extruders. This is costly and complex; thus, it is not suitable for small-batch production [7–12]. Moreover, the prepreg in CFRTC-based FFF printing is predetermined before printing, and the fiber layout and content are fixed, which cannot play a critical matrix role. The second method is in situ impregnation (hereafter referred to as co-extrusion). Continuous fiber bundles and thermoplastic filaments are simultaneously fed into the print head so that the fiber bundles wrapped in a molten thermoplastic matrix material are pulled from the nozzle and deposited on the hotbed [13]. Compared to the prepreg process, this process allows for changes in fiber layout, content, and control of the amount of matrix extrusion dynamically during the printing process.

Whether in the prepreg or co-extrusion process, the surface quality and strength of parts manufactured using the CFRTC-based FFF process are influenced by various process parameters and path planning, such as layer thickness, nozzle diameter, fill spacing, printing temperature, printing speed, matrix feed rate, different fiber materials, and filling strategy [14, 15]. Among these control parameters, it is important to maintain a uniform distribution of matrix material. A larger amount of matrix extrusion causes material

Yingxin Ma, Ling Chen, Lijing Zhang, Huanxiao Wu and Yuan Yao are contributed equally to this work.

✉ Yuan Yao  
yaoyuan@shu.edu.cn

Extended author information available on the last page of the article

stacking, nozzle blockage, and fibers being pulled off under greater resistance. A smaller amount of matrix extrusion cannot fill the actual path void, and the formed samples have insufficient strength and high surface roughness. Therefore, controlling the amount of matrix extrusion was crucial for the overall performance of the samples. In the current study, only few studies have focused on path planning and material extrusion for 3D printing of continuous fiber reinforced polymer composites.

In this study, a co-extrusion control and optimization (CCO) method based on printing speed and deposition path planning is proposed to achieve adaptive extrusion of the matrix during printing of arbitrary samples with different filling paths. CCO method can solve the filling non-uniformity problem, reduce the porosity caused by continuous path planning problems, and improve the quality and mechanical strength of CFRTC-based FFF printing.

## 2 Related works

In the current research on CFRTC-based FFF, the effects of the experimental platform and process parameters on the mechanical properties of the samples have been widely investigated. Goh et al. [16] gave a detailed review of the factors affecting fiber-reinforced printing. They pointed out that although fiber reinforcement can obtain a tensile strength between 83.5 and 143 MPa, it is still lower than the expected strength owing to the poor bonding of the fiber to the matrix. This is mainly because of the ineffective combination of matrix material and reinforcing fibers. The article by Yeong et al. [17] provides a clear and concise discussion of the current status and prospects of fiber-reinforced manufacturing, and reviewed the article by Shi et al. [18], which used the advancing angle of the resin forced the resin to wick toward a high temperature to improve the degree of impregnation of the thermosetting material in the carbon fiber.

Many works are focused on enhancing the quality and strength of samples by optimizing process parameters, improving hardware and strengthen the bonding force between blue intra-layer and inter-layer of the composite material [19, 20]. Tian et al. [21] investigated the effects of process parameters such as temperature, layer thickness, matrix feed rate, printing speed, and deposition spacing on the mechanical properties of the samples based on the co-extrusion process and single variable principle. In addition, by analyzing the relationship between each process parameter and the multi-interface properties of CFRTC, the intrinsic correlations between the process parameters and the interfacial and mechanical properties were established. A higher printing temperature makes the matrix flow faster, and a faster printing speed makes the matrix extrusion insufficient, resulting in

poor bonding. A lower printing temperature slows the matrix flow, and a lower printing speed causes excessive matrix extrusion and poor bonding.

Ueda et al. [22] proposed a 3D compaction printing technique for continuous carbon fiber-reinforced thermoplastics. The hot rollers were configured on a common FFF 3D printer. The compound filaments were compacted onto a hotbed immediately after printing to reduce the porosity and improve the adhesion between the compound filaments. The higher pressure indicates a better density of the molded components, a smaller number of voids, and a higher surface quality. This resulted in a 26% increase in bending strength and a 7% decrease in porosity compared to the untreated compound filament prints. Shuto et al. [23] investigated the effect of nozzle temperature on the transverse tensile strength of CFRTC involved in this study. The strength was higher at higher temperatures and lower at lower temperatures, and the strength decreased with increasing porosity.

Reinforcing fibers have a distinct orthogonal anisotropic structure; therefore, the internal filling path planning of the printed part becomes an important factor affecting the strength and other physical properties. Topology optimization has been used to achieve variable fiber content and layout in continuous Fermat spirals (CFS) [24], Zigzag [25], and Hibbert curves [26].

Huang et al. [27] simultaneously optimized the fiber orientation and topology, redesigned the fiber content by finite element analysis, and changed the continuous fiber path using the layered structure design method as a way to achieve the freedom of continuous fiber-reinforced 3D printing and the improvement of mechanical properties of the samples. McCloud et al. [28] investigated the effect of different raster angles on performance of printed parts. The experimental results show that when the filling direction alternates at  $-45^\circ / +45^\circ$ , the breaking strength is the strongest. Zhang et al. [29] proposed a path planning strategy that guarantees fiber layout orientation aligning with the principal stress direction. The fiber amount fraction was calculated from the obtained fiber trajectory, and then the stress field calculation and fiber trajectory redetermination were performed to obtain the CFRTC-based FFF printing with a variable fiber amount fraction. Hou et al. [30] proposed a stress gradient-based CFRTC distribution to adjust the local fiber orientation and content. After optimization, the ultimate tensile strength is increased by 42%.

Considering the complexity of continuous fiber path planning, many factors can cause the deposition pitch of fiber-reinforced materials to change during printing. These reasons include the complexity of the structure and the properties of the material itself. In 3D printing based on continuous fiber reinforcement, this results in a nonuniform distribution of the matrix material, creating a large number

of internal microscopic pores, which consequently leads to stress concentration and stress transfer, resulting in different structural failure behaviors.

The CCO method proposed in this paper can realize an adaptive adjustment of the amount of matrix extrusion according to the path information and printing speed. This can improve the printing quality and solve the problem of obvious voids existing on the surface of the samples while keeping the path design unchanged. It can not only be used as an offline post-processing method, but can also be combined with online detection technology [31] and embedded in the firmware of the CFRTC printing system to improve printing quality.

### 3 Method

The CCO method is geared toward printing platforms that use in situ impregnation methods to reduce microscopic porosity in printed parts by adjusting the amount of matrix extrusion to compensate for inhomogeneities introduced by the path. It uses a modified in situ co-extrusion head that supports impregnation. First, we used a basic model to calculate the amount of matrix extrusion required for the co-extrusion process. Then, a co-extrusion optimization model was obtained

by adjusting the matrix adaptive extrusion by calculating the geometric deposition spacing.

To guarantee the surface quality and remove the porosity of the print part, the CCO method combines the deposition spacing, printing speed, and fiber characteristics to achieve matrix adaptive extrusion. As a machine-oriented post-processing procedure, it can be applied to various filling paths and complex models. To simplify the model, we ignore the stiffness of the reinforcing fibers themselves, dragging, and other factors in the printing process to bring about deformation, and only consider the uneven distribution of the preset tool path itself.

This method reduces the complexity of the process implementation while improving surface quality and mechanical properties. The framework of the CCO is shown in Fig. 1.

CCO method is divided into three steps: (1) build co-extrusion experiment platform, (2) build co-extrusion basic model, and (3) build co-extrusion optimization model.

#### 3.1 Build co-extrusion experiment platform

By modifying the common desktop-grade FFF printer, the single inlet of the print head was turned into a dual inlet, and the fiber and matrix entered the print head through two inlets. In this study, an extrusion head was designed using

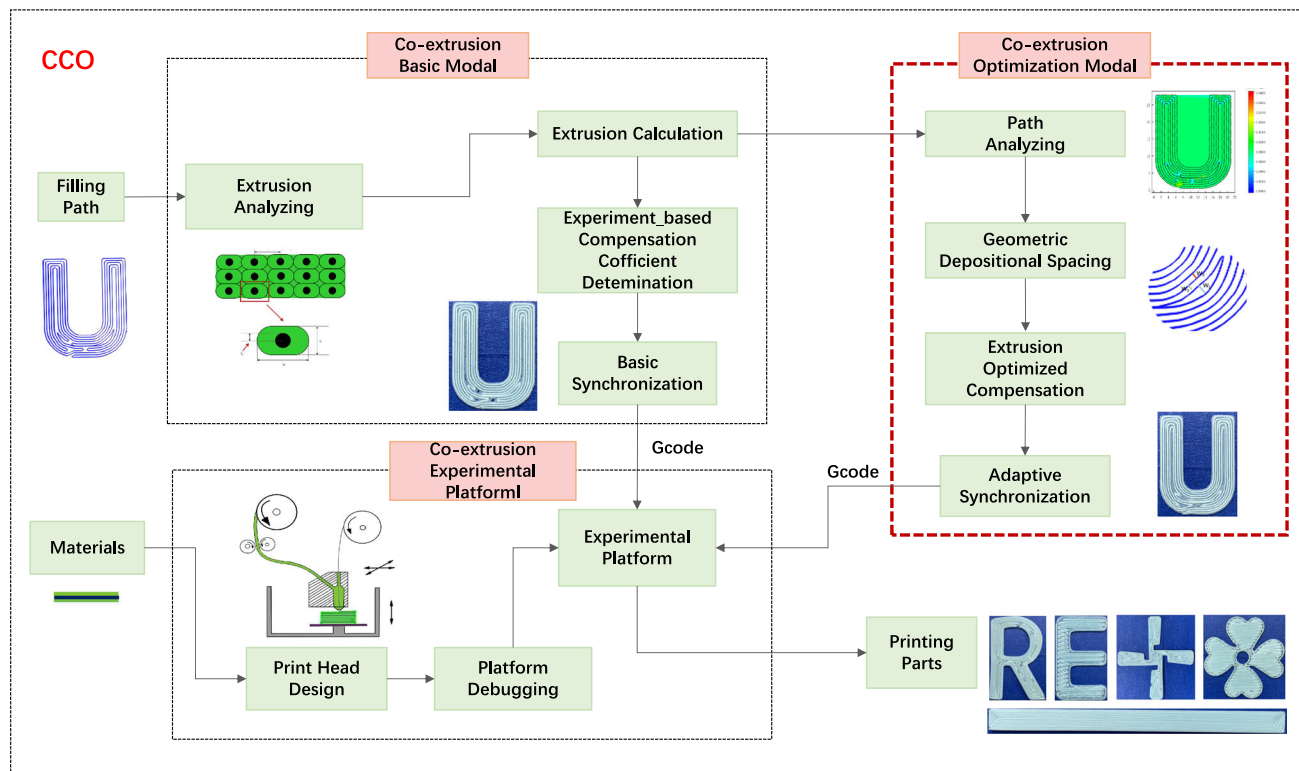


**Fig. 1** Overview of CCO

three different feeding methods to provide better hardware assistance and ensure print quality, as shown in Fig. 2. As shown in Fig. 2a, the matrix material was fed directly into the print head. The molten matrix material enters the through hole and reaches the fibers through a fine tube for impregnation, obtaining CFRTC, and extrusion. The device does not provide a suitable pressure at the print head; a small pressure makes the fibers to be poorly impregnated with the matrix material, and a higher pressure caused the matrix material to overflow. In Fig. 2b, the matrix material is fed into the print head inlet from the slant side, and the through-hole length of the slant side inlet is not less than 5 mm, which provides a larger impregnation space and achieves a better impregnation effect. In Fig. 2c, the matrix material is fed through a lateral back hole perpendicular to the fiber inlet, with the through hole positioned in the middle of the print head. The space for the impregnation of fibers and matrix material in this print head is similar to that in Fig. 2b, but the matrix material is fed into the print head laterally, with more loss and increased experimental error. Therefore, the print head shown in Fig. 2b is used in this study.

In the three print heads, traction pulls the fibers out during printing. It does not use a separate motor configuration, which is simple to operate and simplifies the mechanism. PTFE plastic tubing was then added to the fiber and matrix inlets. Owing to the high-temperature resistance and non-sticking property of PTFE, it can protect the matrix material from premature melting and bonding at the throat. This increases the service life of the entire mechanism.

### 3.2 Basic co-extrusion model

The basic model of co-extrusion provides computational methods for achieving accurate matrix-reinforcement ratio mixing during printing, referred to as the co-extrusion model. First, we conducted global continuous path planning for

a given sample to obtain path information. Subsequently, based on the path and material information, the amount of matrix extrusion corresponding to each printing point was calculated. By combining the experimental platform with the known matrix extrusion volume information, the platform equipment parameters are used to generate synchronization control commands. However, due to factors such as the fiber stiffness, cross-section, extrusion nozzle size, and deposition form, the actual matrix extrusion volume deposited on the platform becomes inaccurate. In paths with high curvature, some molten matrix in its original position may be lost, resulting in uneven printing and poor surface quality. In addition, the matrix material may be unpredictably lost during the printing process (such as residue in the printing head), causing a mismatch between the amount of matrix extrusion and the actual path, resulting in higher porosity of the samples. Therefore, we introduced an experimental compensation coefficient to compensate for the matrix loss.

### 3.3 Co-extrusion optimization

Based on the basic co-extrusion model established in Sect. 3.2, we propose an innovative method to adjust the amount of matrix extrusion according to the actual geometric deposition spacing. This approach can improve the performance and reduce the porosity of the CFRTC-based FFF printing processes. Initially, the path of the sample was analyzed, and the geometric deposition spacing was calculated for every printing point. The amount of matrix extrusion was then recalculated for each point depending on the geometric deposition spacing. To avoid printing instability that may arise from matrix extrusion mutations, matrix extrusion smoothing is performed using convolution operations. Considering the time lag of the motor delivering the substrate material, the amount of matrix extrusion was then optimized using interpolation to reduce the inaccuracies caused by the printing

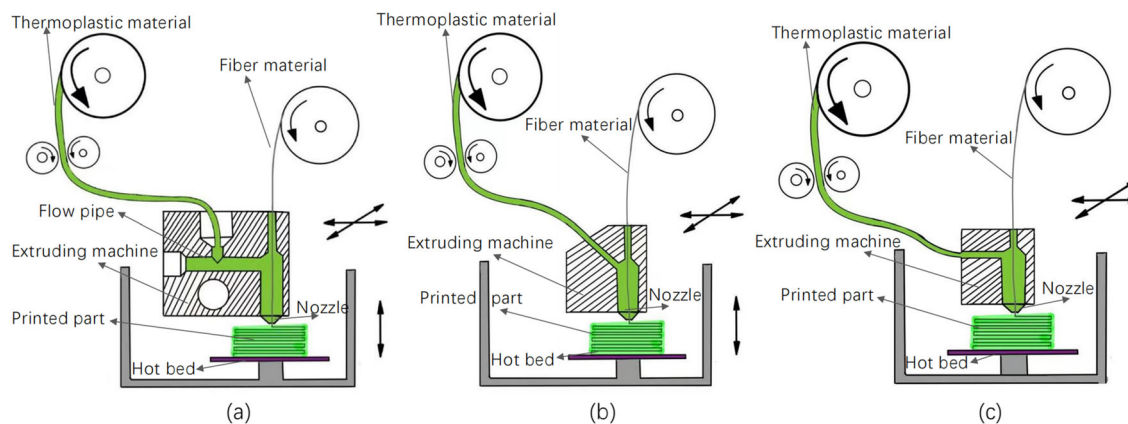


**Fig. 2** Print head design for co-extrusion experimental platform. **a** Matrix material is fed into the print head from directly above inlet. **b** Matrix material is fed into the print head from the side inlet. **c** Matrix material is fed into the print head from the behind inlet

hysteresis. By optimizing the amount of matrix extrusion to align with the actual path voids, the porosity can be reduced and the mechanical properties of the printed samples can be enhanced.

## 4 Co-extrusion model

In this paper, we refer to the work of Hou et al. [30] to address the problem of matrix material input and output in the print head. The total volume of the matrix entering the print head and the total volume of the extruded print head were equal in macroscopic terms.

### 4.1 Calculation of matrix extrusion amount

The extrusion process of the matrix during printing is shown in Fig. 3. We assumed that the cross-section of the composite material deposited on the hotbed was approximately rectangular and that of the fiber material was circular. The total amount of matrix extrusion fed into the print head per unit of time can be expressed as the product of the length of the matrix material fed and its cross-sectional area, as shown in Eq. 1.

$$V_1 = \pi * r_m^2 * v_e \quad (1)$$

Here,  $V_1$  is the total amount of matrix extrusion being fed into the print head per unit of time,  $v_e$  is the wire feed speed of the matrix material extruder, and  $r_m$  is the radius of the cross-section of the matrix material.

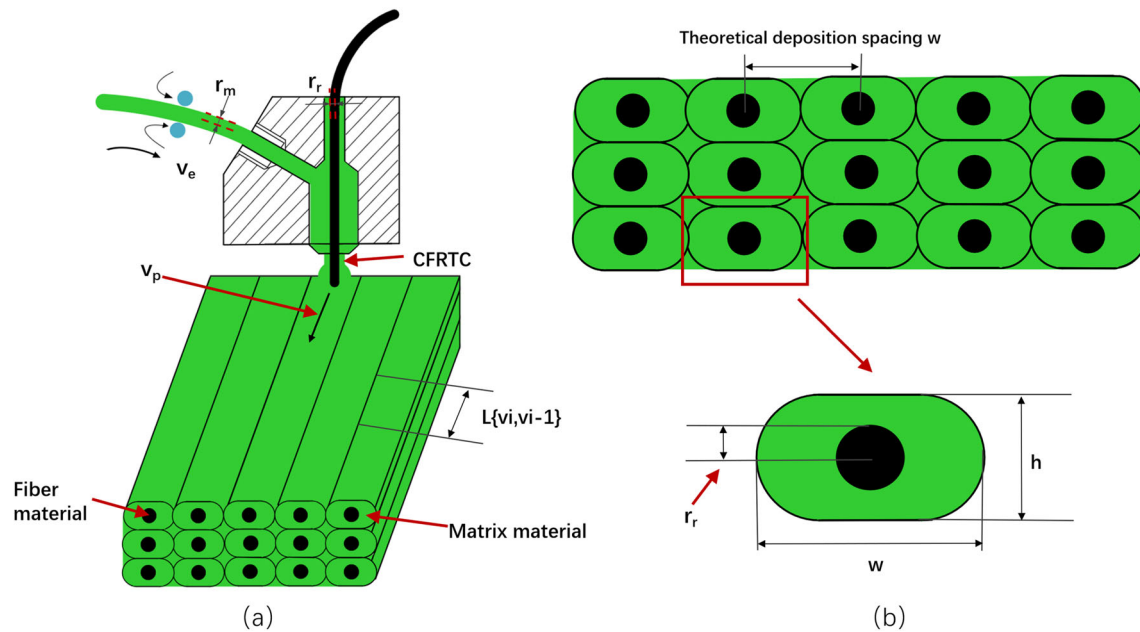


**Fig. 3** Schematic of sample printing. **a** Illustration of material extrusion. **b** Cross-section of composite materials

The total amount of matrix extrusion extruded into the print head per unit of time should be the total amount of the composite material of any length of the printed part minus the total amount occupied by the fibers, as in Eq. 2.

$$V_2 = h * w * v_p - \pi * r_r^2 * v_p \quad (2)$$

$V_2$  is the total amount of matrix extrusion from the print head per unit of time,  $h$  is the print thickness,  $w$  is the width of a single composite material deposited on the print platform,  $v_p$  is the speed of nozzle movement, and  $r_r$  is the fiber radius.

From the law of conservation of mass, it is known that  $V_1 = V_2$ , i.e., Eq. 3.

$$\pi * r_m^2 * v_e = h * w * v_p - \pi * r_r^2 * v_p \quad (3)$$

Therefore, it is possible to calculate the wire feed speed of the matrix material extruder  $v_e$  when printing a composite sample of any length, i.e., Eq. 4.

$$v_e = \frac{h * w - \pi * r_r^2}{\pi * r_m^2} * v_p \quad (4)$$

Consider that the actual input and extruded matrix materials are not equal, such as matrix spillage and amount change due to temperature change during printing. Therefore, a compensation coefficient  $\lambda$  is introduced.

$$\lambda * V_1 = V_2 \quad (5)$$

Then,

$$v_e = \frac{h * w - \pi * r_r^2}{\lambda * \pi * r_m^2} * v_p \quad (6)$$

In Gcode, the amount of matrix extrusion is typically set using the  $E$  parameter, and when using the absolute mode,  $E$  is calculated by Eq. 7.

$$E = E(v_e) = v_e * L\{v_i, v_{i+1}\} \quad (7)$$

$v_i$  and  $v_{i+1}$  are the printing velocity of any point in the path and the point after it, respectively, and  $L\{v_i, v_{i+1}\}$  denotes the length between any two points.

## 4.2 Compensation coefficient

Due to matrix loss, a compensation coefficient  $\lambda$  needs to be introduced between the matrix input and output. On a modified co-extrusion printing platform, appropriate process parameters such as layer thickness, printing temperature, and printing speed are crucial for successful printing. Printing speeds that are too high can lead to inadequate impregnation of continuous fibers with the matrix and insufficient matrix extrusion, resulting in voids and poor print quality. Conversely, printing speeds that are too slow can cause the molten matrix to spill out, potentially solidifying at the fiber entrance and leading to continuous fiber breakage or excessive matrix build-up on the sample surface. Low temperatures can also reduce the mobility of the matrix material, diminish the fiber and matrix impregnation effect, or even affect

composite cooling. Therefore, suitable process parameters are the prerequisites for introducing  $\lambda$ . This paper presented the printing of various process parameters based on the co-extrusion process, as shown in Table 1.

As shown in Table 1, selecting the appropriate process parameters is crucial for successful printing on modified co-extrusion printing platforms. When the layer thickness of 0.1 mm, the nozzle is too close to the hotbed, resulting in clogging of the matrix in the nozzle. Conversely, when the layer thickness exceeds 0.5 mm, the nozzle is too far from the hotbed, and the composite material has difficulty adhering to the hotbed. Printing speeds below 80 mm/min result in slow printing and matrix clogging, while printing speeds over 240 mm/min and printing temperatures over 220°C make it difficult for the composite material to adhere to the hotbed.

For a more intuitive feeling of successful printing in the range of process parameters, we drew a histogram of the printing situation under changes in process parameters. This is shown in Fig. 4. From the graph, we can conclude that the layer height should be between 0.2 and 0.4 mm, the printing temperature should be between 180 and 220°C, and the printing speed should be between 80 and 240 mm/min which can be printed successfully. However, there are mutation paths in complex samples; the printing speed of the mutation path is 80 mm/min, and the printing speed of the linear path is 180 mm/min, which not only ensures the stability of printing but also improves the efficiency. In this study, the following process parameters were used: layer height of 0.3 mm, linear path printing speed of 180 mm/min, mutation path printing speed of 80 mm/min, printing temperature of 190 °C, hotbed temperature of 50 °C, and nozzle diameter of 0.6 mm.

Experiments were conducted to determine the complementary coefficients based on the aforementioned process parameters. The results indicate that, when  $\lambda < 0.76$ , the amount of matrix extrusion is insufficient to allow the compound to adhere to the hotbed. Thus, the appropriate range for the compensation coefficient is  $0.76 < \lambda < 1$ . It is important to note that  $\lambda < 1$  because the total amount of matrix extrusion entering the print head always exceeds the total amount of matrix extrusion extruded from the print head.

## 4.3 Basic model printing

Five samples were printed using a basic model. The sample path in Fig. 5 is filled with CFS, with a deposition spacing of 0.3 mm. From Fig. 5a, it can be seen that the deposition spacing is inconsistent, with larger spacing in adjacent paths in the red region and smaller spacing in adjacent paths in the brown region. As shown in Fig. 5b, the actual printed sample had too much matrix in the brown region, resulting in stacking, and too scanty matrix in the red region, resulting in voids. In Fig. 6a, increasing the deposition spacing to 0.6 mm made the unevenness problem more pronounced.

**Table 1** Process parameter experiment

Layer height (mm)	Printing speed (mm/min)	Temperature (°C)	Printability
0.1	40	180	Clogged
0.2	40	180	Clogged
0.3	40	180	Damaged
0.4	40	180	Damaged
0.5	40	180	Not attached
0.6	40	180	Not attached
0.2	80	180	Damaged
0.2	120	180	Printable
0.2	160	180	Printable
0.2	200	180	Printable
0.2	240	180	Printable
0.2	280	180	Not attached
0.2	80	200	Printable
0.2	80	220	Printable
0.2	80	240	Damaged

**Fig. 4** Experimental results of different process parameters

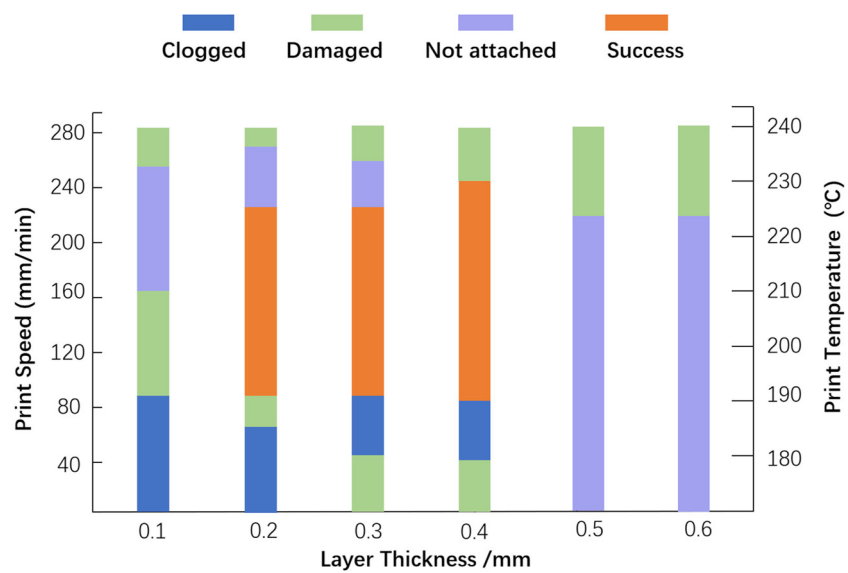


**Fig. 5** Letter U with 0.3 mm deposition spacing. **a** Filling pattern. **b** Actual sample

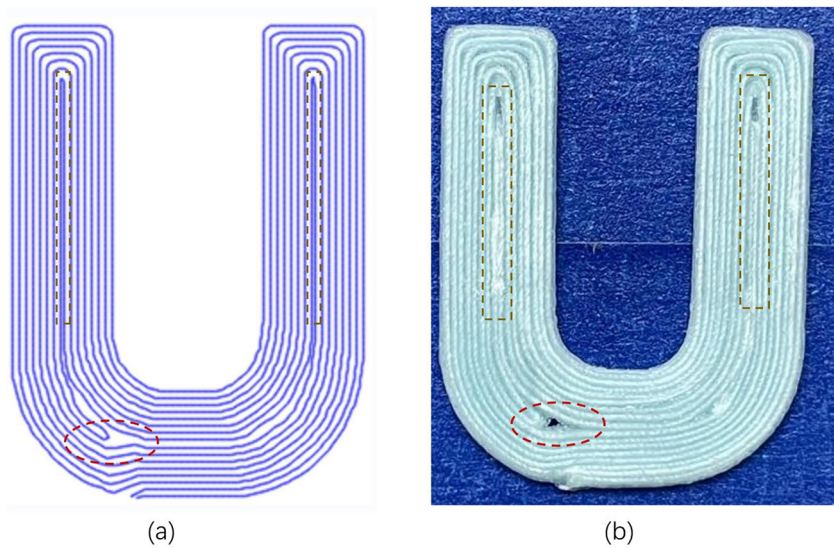


**Fig. 6** Letter U with 0.6 mm deposition spacing. **a** Filling pattern. **b** Actual sample

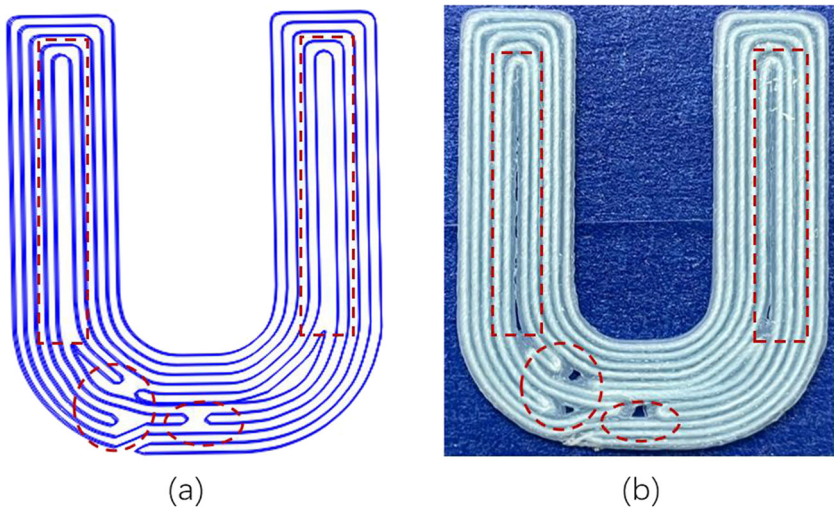
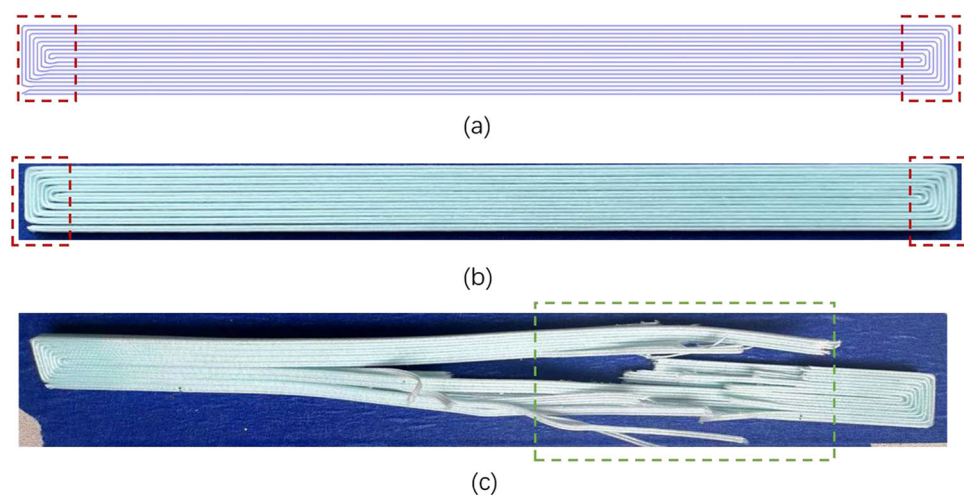


**Fig. 7** Tensile samples with 0.7 mm deposition spacing. **a** Filling pattern. **b** Actual sample. **c** Sample parts after tensile fracture



From Figs. 5 and 6, it can be seen that there is a problem of uneven deposition spacing in the globally continuous CFS-filled path, which leads to underfilling or overfilling of the samples. When using CFS to fill the stretched standard part with a deposition spacing of 0.7 mm, the deposition spacing in the red region of the path underwent a sudden change, and voids appeared in the corresponding area of the actual sample, as shown in Fig. 7b. When the sample was stretched to fracture, the fracture surface was uneven and the composite material was pulled apart, as shown in Fig. 7c. This is because the amount of matrix extrusion is insufficient, resulting in inadequate bonding strength between and within the layers and uneven stress distribution in different regions of the sample. Figure 8 shows a sample printed with CFS infill and a deposition spacing of 0.55 mm. Although the deposition spacing in the path is basically even, during the actual printing process, due to the rigidity and continuity of the fibers, the fibers deviate from the predetermined path and remove some of the matrices. This resulted in uneven edge filling, as shown in the yellow area in Fig. 8b.

As shown in Fig. 9, in the Zigzag-filled sample containing holes, with a deposition spacing of 0.7 mm, the areas with uneven deposition spacing increased. In Fig. 9b, there was an obvious void in the red region. Because the printing of the sample ended from the top red region, there was a continuous

composite material (orange region) in the actual print, which filled the voids in the top red region.

In samples with global continuous paths, both CFS and Zigzag filling suffer from uneven deposition spacing. The basic model cannot adaptively fill surface voids based on the actual geometric deposition spacing, which can lead to underfilling and overfilling. In addition, fiber rigidity can cause the fiber to deviate from a predetermined path, expand or shrink surface voids, and cause printing instability.

## 5 Optimization model

The optimization model mainly achieves adaptive extrusion of the matrix based on the geometric deposition spacing. The actual geometric deposition spacing of each point was obtained based on the path information, and the amount of matrix extrusion was updated accordingly. To ensure stable printing, a convolution operation was used to process the abrupt changes in the extrusion amount. During the printing process, the extrusion and input of the matrix cannot be synchronized, and interpolation is used to solve the delay in the amount of matrix extrusion. This process is illustrated in Fig. 10.

**Fig. 8** Windmills with 0.55 mm deposition spacing. **a** Filling pattern. **b** Actual sample

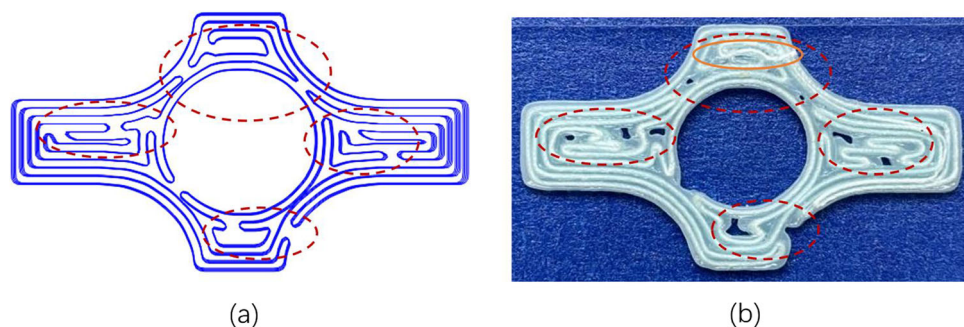
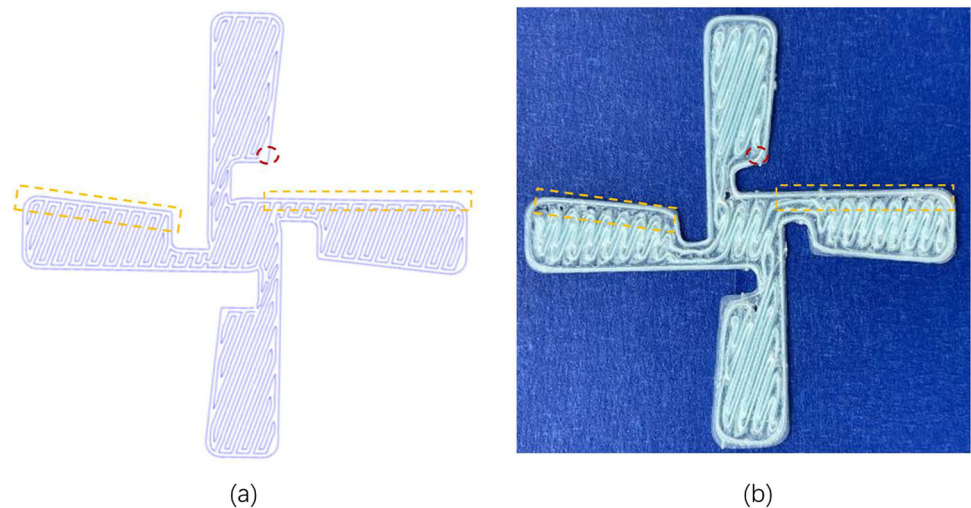


**Fig. 9** Crucifixion with 0.7 mm deposition spacing. **a** Filling pattern. **b** Actual sample



### 5.1 Optimal control of co-extrusion

The deposition spacing of the printed path and the intended path was not exactly the same in some areas. First, the nearest-neighbor algorithm is used to obtain the neighborhood point set for each point on the adjacent path. The topological relationship between the points was obtained by analyzing the point set. Subsequently, based on the topological relationship of the point set, the geometric deposition spacing  $W'_i(v_e)$  of the corresponding point is calculated. Finally, a fitting function is used to make the deposition spacing  $W_i(v_e)$  of the corresponding point in the basic model approach infinitely close to  $W'_i(v_e)$  and update the corresponding amount of

matrix extrusion. The fitting function is given by Eq. 8.

$$\arg \min_{v_e} \frac{1}{2n} \sum_{i=1}^n (W'_i(v_e) - W_i(v_e))^2 \quad (8)$$

### 5.2 Topological relationship of point set in neighborhood

To analyze the topological relationship of the fill paths, the input fill paths need to be sampled accurately. First, a path point  $p$  is selected as the target point, and threshold  $k$ . Second, a nearest-neighbor search is performed with point  $p$  as the center and  $k$  as the radius to find a set of points in the

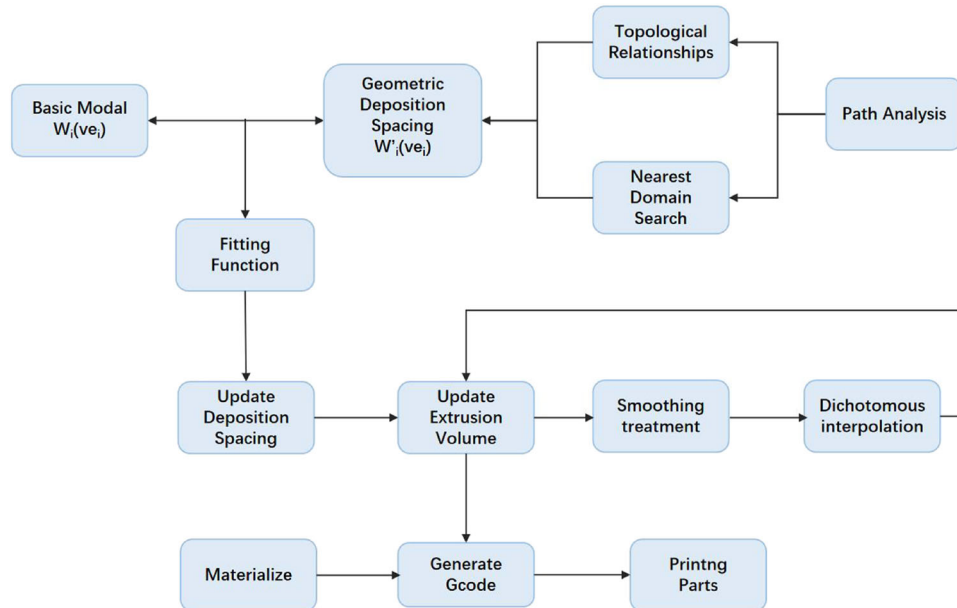


**Fig. 10** Flow chart of the optimization model

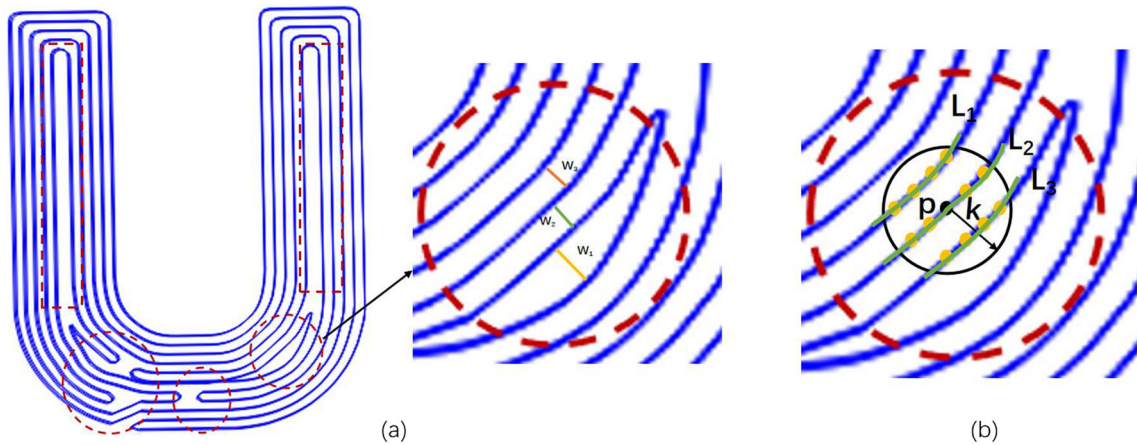


**Fig. 11** Modal path. **a** Filling pattern. **b** Point set in neighborhood and topological relationship

neighborhood of point  $p$ , as indicated by the bright yellow dots in Fig. 11b. To find as many points in the neighborhood as possible and to improve the accuracy of the data, the larger the value of  $K$ , the better.  $k$  is generally set between 1.2 and 1.8  $w$  ( $w$  represents the size of the deposition spacing). When  $k < 1w$ , the neighborhood circle may not intersect with the adjacent path of  $p$ , and the required points cannot be found. When  $k > 2w$ , the neighborhood circle is too large, and the point set contains points on nonadjacent paths, which increases the complexity of subsequent calculations. Second, the topological relationship of the point set was determined. Based on the characteristics of the points and the path relationship, the points on the same path are stored together, as shown by the three green paths in Fig. 11b.

### 5.3 Calculate geometric deposition spacing

The geometric deposition spacing during the printing process is determined based on the nearest-neighbor points and their topological relationships in the neighborhood of the target point  $p$ , as discussed in Sect. 5.3. To calculate this spacing, we traverse the other neighborhood point sets, except for the path where  $p$  is located, and calculate the straight-line distance between  $p$  and the two adjacent paths. The weighted average of these distances was considered the geometric deposition spacing of  $p$ .

**Fig. 12** Two types of adjacent deposition distances. **a** Point set in neighborhood. **b** Two domain points can be found on both adjacent paths. **c** Only one domain point can be found on either adjacent path

There are two situations in the distribution of point sets: the first is when the target point is known and two adjacent paths can be found, and the second is when only one adjacent path can be found, or no adjacent paths can be found. In the first situation, traverse all point sets on the adjacent path  $L_i$  and calculate the straight-line distance between them and  $p$ . The distances are then sorted from small to large, and the points  $p_{i-1}$  and  $p_i$  correspond to the minimum and second-smallest distances, respectively. Using the same method, we determined the points  $p_{j-1}$  and  $p_j$  corresponding to the minimum and second-smallest distances on the adjacent path  $L_j$ , as shown in Fig. 12a. Second, a line  $L_m$  was drawn through  $p_{i-1}$  and  $p_i$ , and the perpendicular distance from  $p$  to this line was calculated and denoted by  $w_1$ . Line  $L_n$  was drawn through  $p_{j-1}$  and  $p_j$ , and the perpendicular distance from  $p$  to this line was calculated and denoted by  $w_2$ , as shown in Fig. 12b. Because the matrix was uniformly deposited on both sides of the path after it was extruded from the nozzle, the extrusion of the matrix on adjacent paths affected each other. Using the weighted average, the weighted average of  $w_1$  and  $w_2$  is taken as the actual geometric deposition spacing  $w$  of  $p$  in the actual printing process. Due to the irregularity of the entire continuous path, there may be a situation where there is only one path point on the adjacent path, as shown in Fig. 12c. In this case, the straight-line distance between the point and  $p$  was used as  $w_2$ , and the average of  $w_1$  and  $w_2$

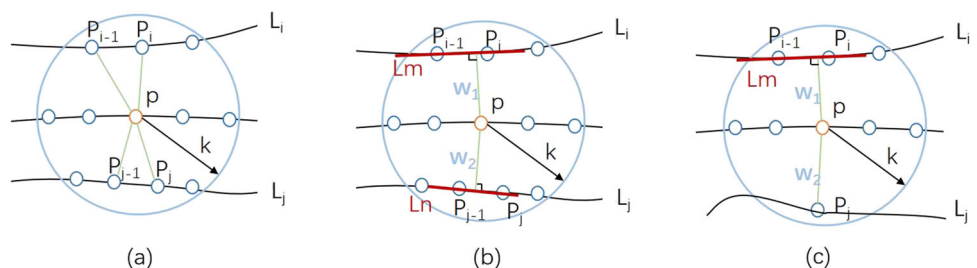
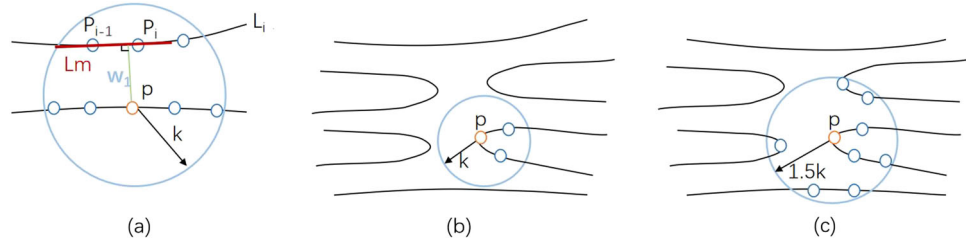


**Fig. 13** Special case of deposition spacing. **a** The target point is on an edge path. **b** No domain point can be found on the adjacent path. **c** Expand K until the domain point is found on the adjacent path



was taken as the geometric deposition spacing  $w$  of  $p$  in the actual printing process.

In the second case, as illustrated in Fig. 13, when  $p$  is on the edge path, only one adjacent path can be found. The point set on this path is traversed, and  $p_{i-1}$  and  $p_i$  using the method described earlier. We then drew a straight-line  $L_n$  passing through  $p_{i-1}$  and  $p_i$ . The straight-line distance between  $p$  and  $L_n$  was calculated and used as the actual geometric deposition spacing of  $p$  during the printing process, as shown in Fig. 13a. If  $p$  is not on the edge path and no adjacent path can be found, the value of  $k$  in the ANN algorithm increases. An increase in  $k$  by 1.5 times a time until the neighborhood circle can intersect with other paths, and other neighborhood points can be found, as shown in Fig. 13c. After finding the other neighborhood points, the deposition spacing was calculated using the method described earlier.

#### 5.4 Amount of matrix extrusion

As previously mentioned, the formula for calculating the feed rate per unit time is known. Based on the change in the geometric deposition spacing, the updated calculation is shown in Eqs. 9 and 10.

$$v'_e(i) = \frac{h * w(i) - \pi * r_r^2}{\lambda * \pi * r_m^2} * v_p, i = 1, 2, \dots, n \quad (9)$$

$$E = E(v'_e) = v'_e * L\{v_i, v_{i-1}\} \quad (10)$$

After recalculating the amount of matrix extrusion, large fluctuations can cause printing instability and uneven surfaces. Therefore, the amount of extrusion must be smoothed. In this study, a convolution was used to smooth the extrusion. As shown in Eq. 11, a discrete Gaussian function  $g(k, \sigma)$  is given with  $\sigma$  as the standard deviation. Here,  $\sigma = 0.02$  and  $l = 5$ .  $g(k, \sigma)$  represents the  $k$ th value and  $e(n-k)$  represents the extrusion amount at position  $n - k$ .

$$E(n, k) = \sum_{k=-l}^{k=l} e(n-k)g(k, \sigma) \quad (11)$$

After the matrix is fed into the print head, it cannot be immediately extruded from the print head, which causes a time delay. Interpolation is used to insert half of the extrusion amount at the  $i + 1$ th point between the  $i$ th and  $i + 1$ th points, in order to advance the extrusion amount of the  $i + 1$ th point. Because the path has already been determined, the interpolated value is assigned to the extrusion amount of the  $i$ th point, as shown in Eq. 12.

$$E_i = \frac{1}{2}(E_i + E_{i+1}) \quad (12)$$

The five sample parts in Sect. 4.3 were printed using an optimization model. Figure 14a and b show the sample printed by the basic model and the corresponding matrix extrusion maps. Figure 14c and d show the sample printed by

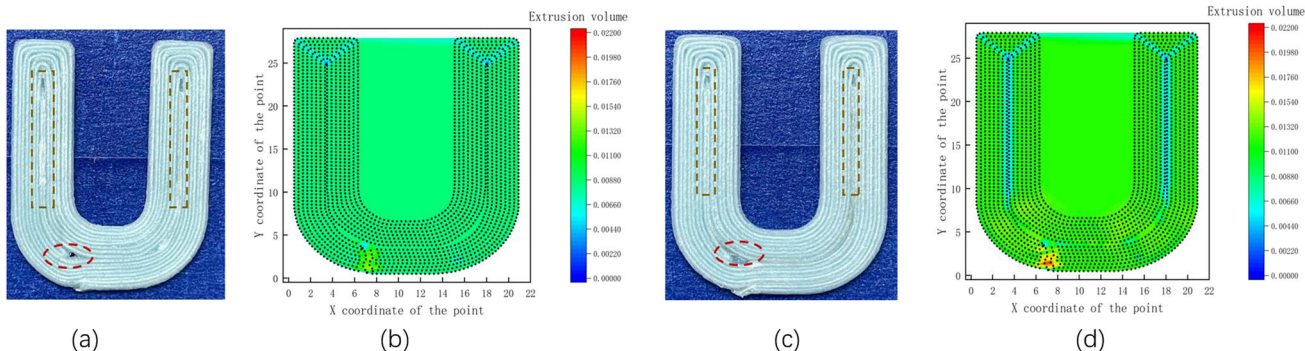


**Fig. 14** Results of letter U with 0.3 mm deposition spacing. **a** Basic model printed prototypes. **b** Matrix extrusion contour maps of the sample printed by the basic model. **c** Optimization model printed prototypes. **d** Matrix extrusion contour maps of the sample printed by the optimization model

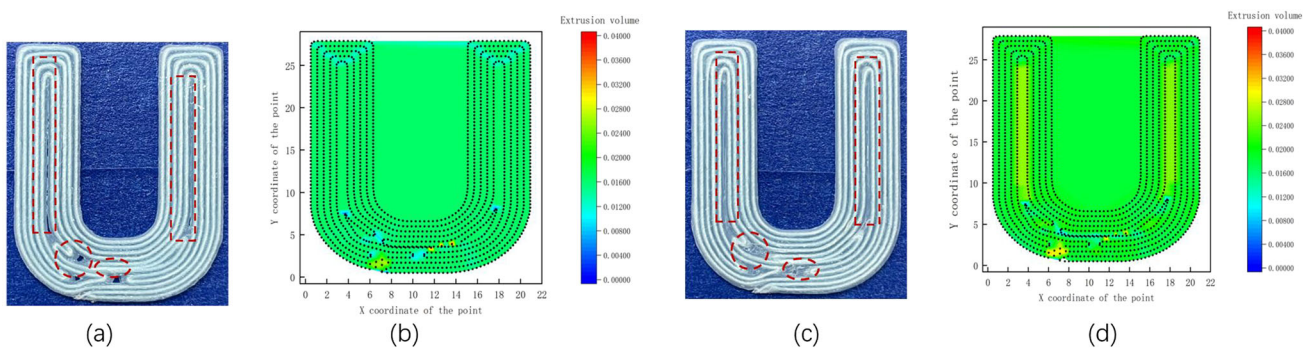
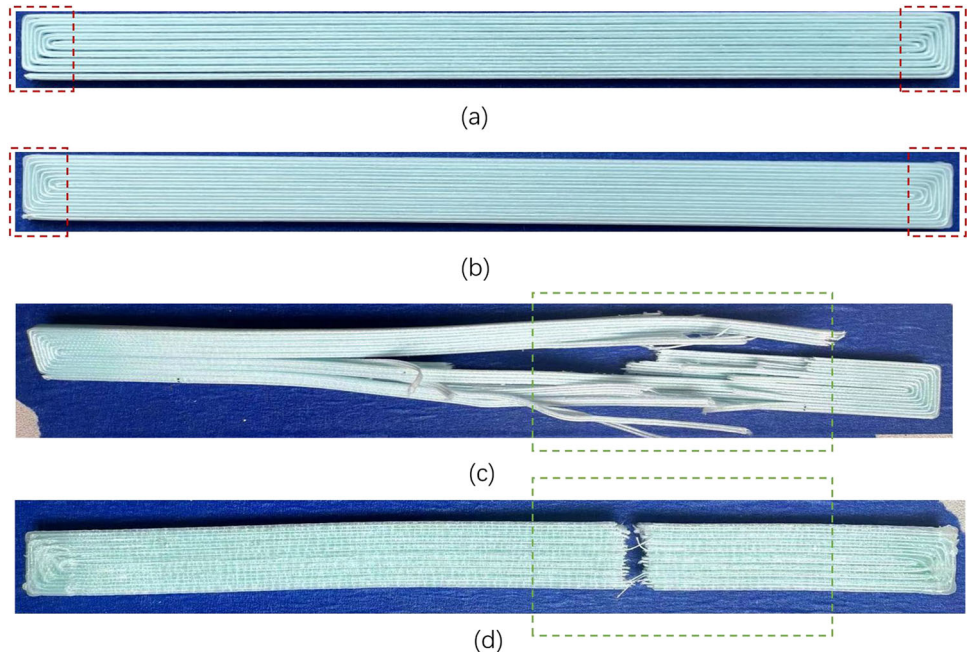


**Fig. 15** Results of letter U with 0.6 mm deposition spacing. **a** Basic model printed prototypes. **b** Matrix extrusion contour maps of the sample printed by the basic model. **c** Optimization model printed prototypes. **d** Matrix extrusion contour maps of the sample printed by the optimization model

the optimization model and their corresponding matrix extrusion maps. From Fig. 14a and c, it can be observed that the sample printed by the basic model was over-extruded in the brown region and under-extruded in the red region, whereas the sample printed by the optimization model reduced the matrix extrusion in the over-extruded region and increased it in the under-extruded region. In Fig. 14d, the over-extruded region is shown in blue and the under-extruded region is shown in red. In Fig. 15a and c, it can be seen that the sample printed by the optimization model can effectively fill the under-extruded regions of the sample printed by the basic model. The corresponding matrix extrusion maps show that the under-extruded regions in the basic model are shown in cyan, whereas those in the optimization model are shown in yellow, indicating an increase in matrix extrusion. Compare to Fig. 16a and c, it can be seen that the matrix extrusion of

the stretching sample printed by the optimization model is more uniform than that of the stretching sample printed by the basic model, and the under-extruded region has been filled. The increase in matrix extrusion enhanced intra- and inter-layer bonding, preventing composite material pull-out during sample fracture. Because the basic model did not implement an adaptive adjustment of the amount of matrix extrusion, the sample shown in Fig. 17 shows green in both over-extruded and under-extruded regions. In contrast, in Fig. 17d, the over-extruded region is shown in blue, and the matrix extrusion is reduced; the under-extruded region is shown in yellow, and the matrix extrusion is increased. In the last sample in Sect. 4.3, the global deposition distances were generally equal. However, owing to the rigidity and continuity of the fibers, some of the matrix was taken away from the edge, resulting in an uneven surface filling of the sample, as shown

**Fig. 16** Results of tensile samples with 0.7 mm deposition spacing. **a** Basic model printed prototypes. **b** Fracture of the sample printed by the basic model. **c** Optimization model printed prototypes. **d** Fracture of the sample printed by the optimization model



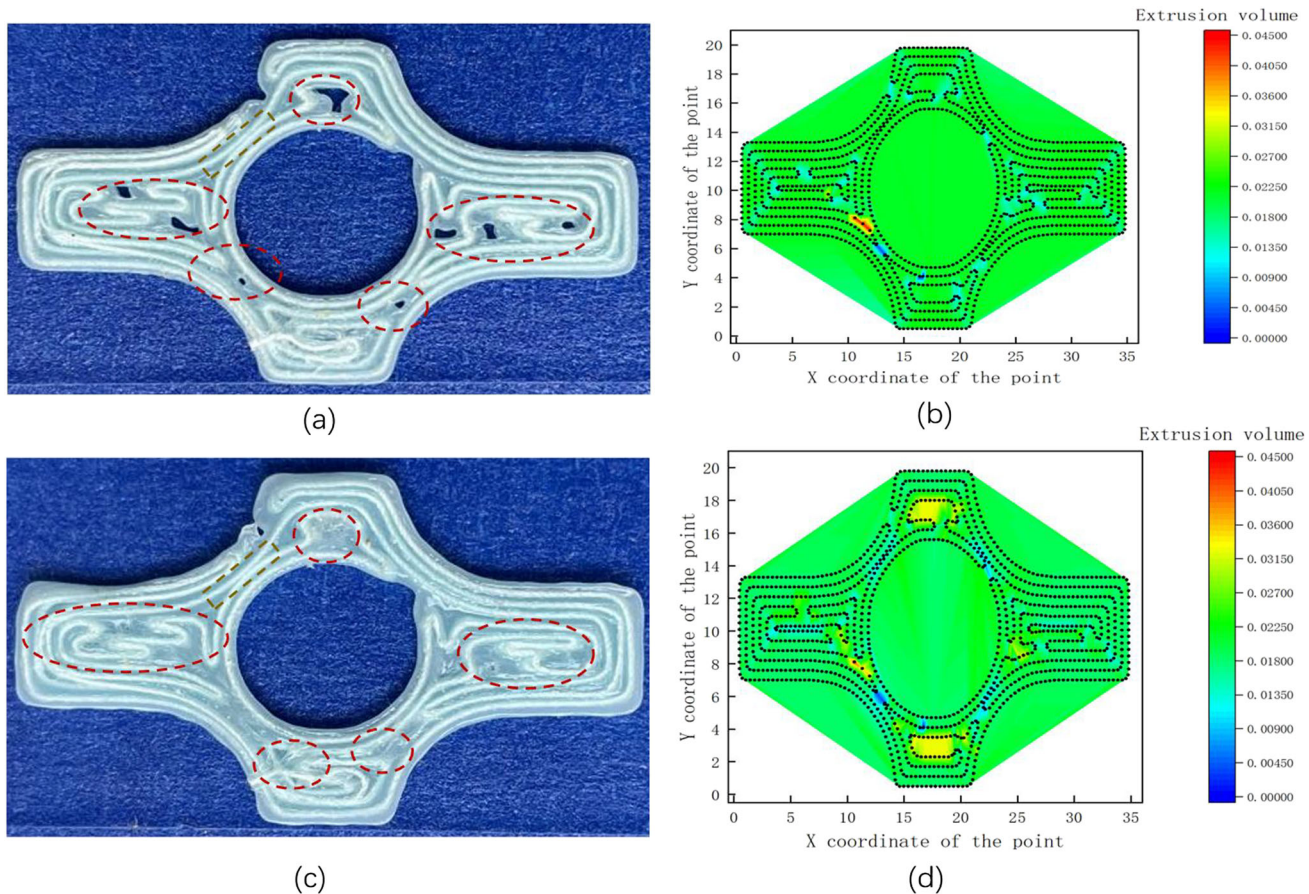


**Fig. 17** Results of crucifixion with 0.7 mm deposition spacing. **a** Fracture of the sample printed by the basic model. **b** Matrix extrusion contour of the sample printed by the basic model. **c** Optimization model printed prototypes. **d** Fracture of the sample printed by the basic model by the optimization model

in Fig. 18a. In the optimized model, the overall matrix was optimized and the sample was filled uniformly in the corresponding areas.

In samples with globally continuous paths, whether using CFS or Zigzag filling, the optimized model can adaptively adjust the amount of matrix extrusion based on the path information to improve the uneven filling and printing quality.

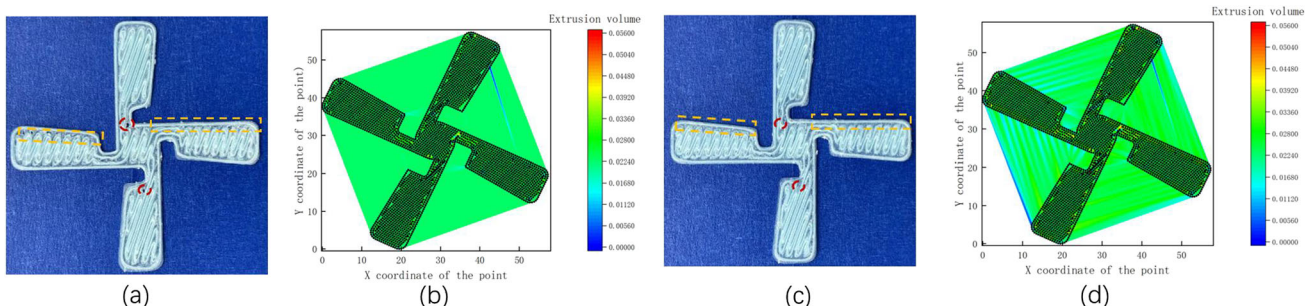


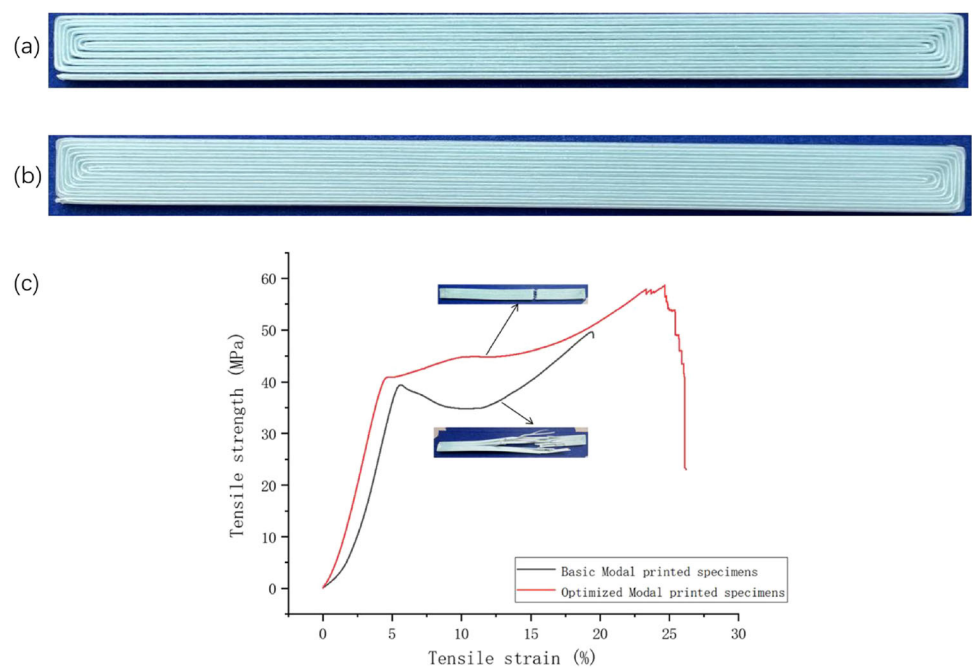
**Fig. 18** Results of windmills with 0.55 mm deposition spacing. **a** Fracture of the sample printed by the basic model. **b** Matrix extrusion contour of the sample printed by the basic model. **c** Optimization model printed prototypes. **d** Fracture of the sample printed by the basic model by the optimization model

## 6 Experiment and discussion

### 6.1 Tensile test

The tensile samples were made of ASTM D3039 standard, polyethylene terephthalate (PET) with a diameter of 0.2 mm

**Fig. 19** Tensile test results. **a** Basic model printed prototypes. **b** Optimization model printed prototypes. **c** Schematic diagram of tensile test strength results



as the fiber material, and polylactic acid (PLA/1.75 mm) as the matrix material.

The experimental results are presented in Fig. 19, the samples were prepared using CFS-filled paths with a deposition pitch of 0.6mm. The voids in the basic model could be reduced by preparing a sample from the optimized model. The tensile strength of the basic model printed sample was 50 MPa, and the optimized tensile strength was 59 MPa, an improvement of 18%. In Fig. 19c, the tensile strength decreases slightly in the middle. This is due to insufficient matrix extrusion and poor intra- and inter-layer bonding in the basic model, which resulted in the withdrawal of the composite filament.

## 6.2 Bending test

A three-point bending test sample was adopted from the GB/T 1449 standard. Experimental results are shown in Fig. 20. The trends of the bending strength and tensile strength were basically the same, and the surface voids of the optimized sample were improved. The bending strength and modulus of the basic model were 64 MPa and 2.9 GPa respectively, whereas those of the optimized model were 79 MPa and 3.6 GPa respectively. Compared with the basic model, the strength and modulus were improved by 23.4% and 24.1%, respectively. The results show that the bending strength of the sample was improved to a certain extent after the optimization of the matrix extrusion.

## 6.3 Microstructures

In composites, the quality of the interfacial impregnation between fibers and matrix directly affects the mechanical properties of the composite. Scanning electron microscopy (SEM) was used to examine the internal structures of the samples. The SEM images of the fracture section of the specimen, the fracture surface of the single composite, and the surface at the corner path are shown in Fig. 21. Porosity was calculated from the cross-sectional SEM images using ImageJ software by dividing the area of the voids (darker areas) by the total area to obtain the void fraction. The fiber fraction was calculated using a weight ratio algorithm.

It can be seen from Fig. 21a and b that the cross-sections of the tensile samples at fracture that the samples prepared by the basic model have more pores between the filaments in the cross-section at fracture, and the porosity is about 28.9% after ImageJ calculation, while the optimized model has less pores between the filaments, and the porosity is 15.7%. As seen from Fig. 21c and d, the single filament fracture diagrams, the composite prepared by the basic model fractured with loose fibers and most of the PLA peeled off from the fiber filaments, while the composite prepared by the optimized model was fractured with compact fibers. From Fig. 21e and f, the surfaces of the tensile samples at the corners, it can be seen that there is insufficient matrix extrusion in the basic model and only a small amount of residual matrix on the fiber surface at the corners of the samples, while more matrix remains on the fiber surface in the optimized model. Due to

**Fig. 20** Bending test results. **a** Basic model printed prototypes. **b** Optimization model printed prototypes. **c** Schematic diagram of Bending test strength results

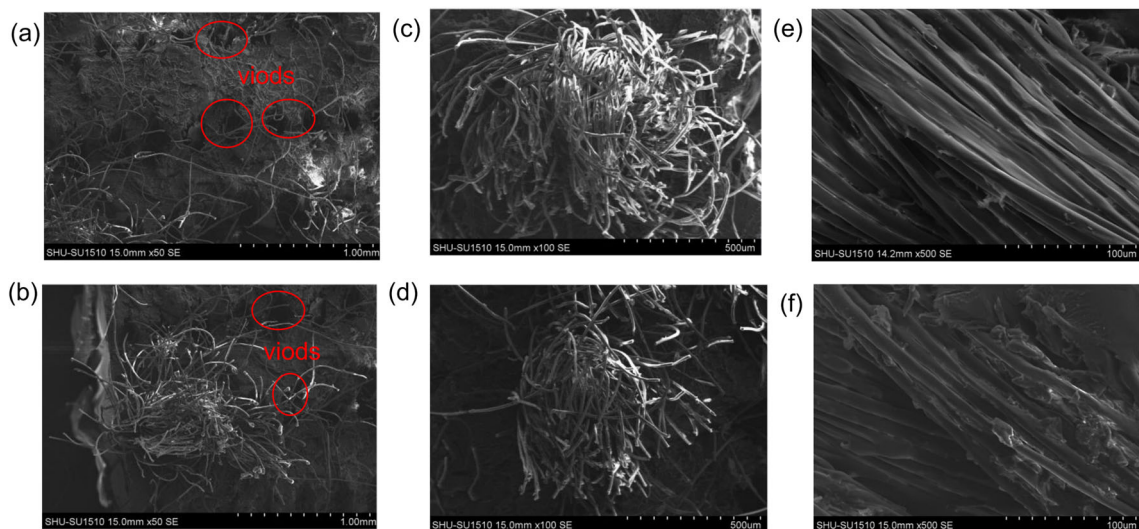
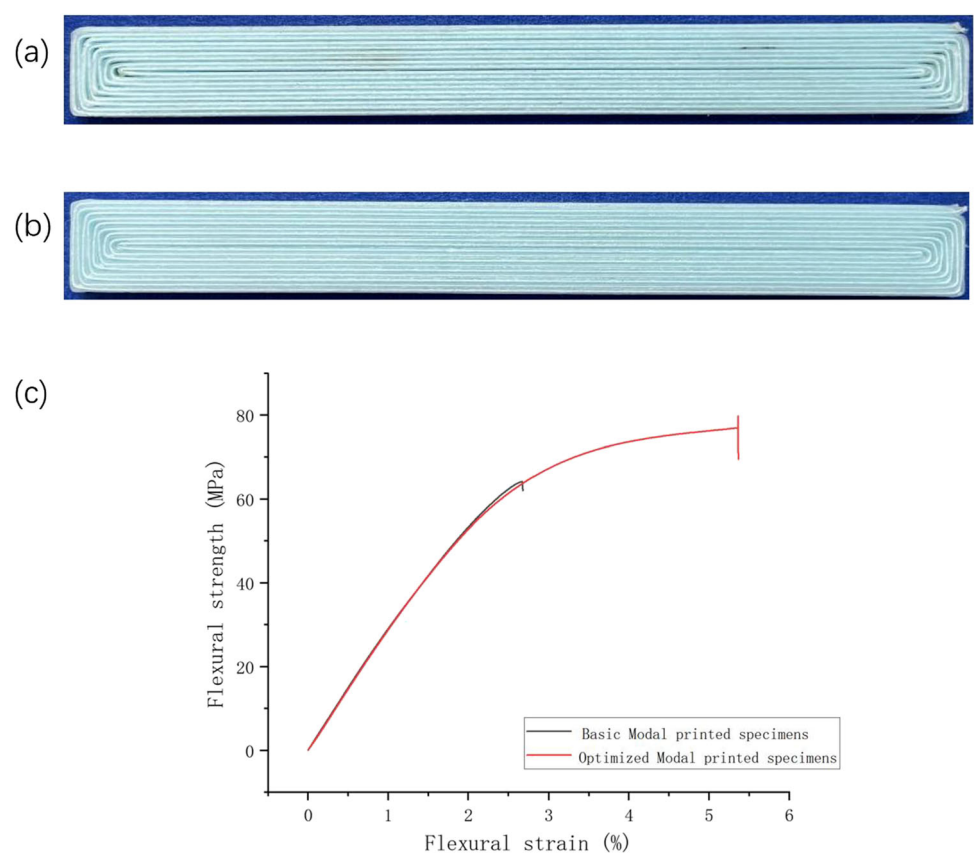


**Fig. 21** Microstructures of PET reinforced PLA specimens. **a** The cross-section of the sample part fracture before optimization. **b** The cross-section of the sample part fracture after optimization. **c** Single

composite cross-section before optimization. **d** Single composite cross-section after optimization. **e** Single composite corner surface before optimization. **f** Single composite corner surface after optimization

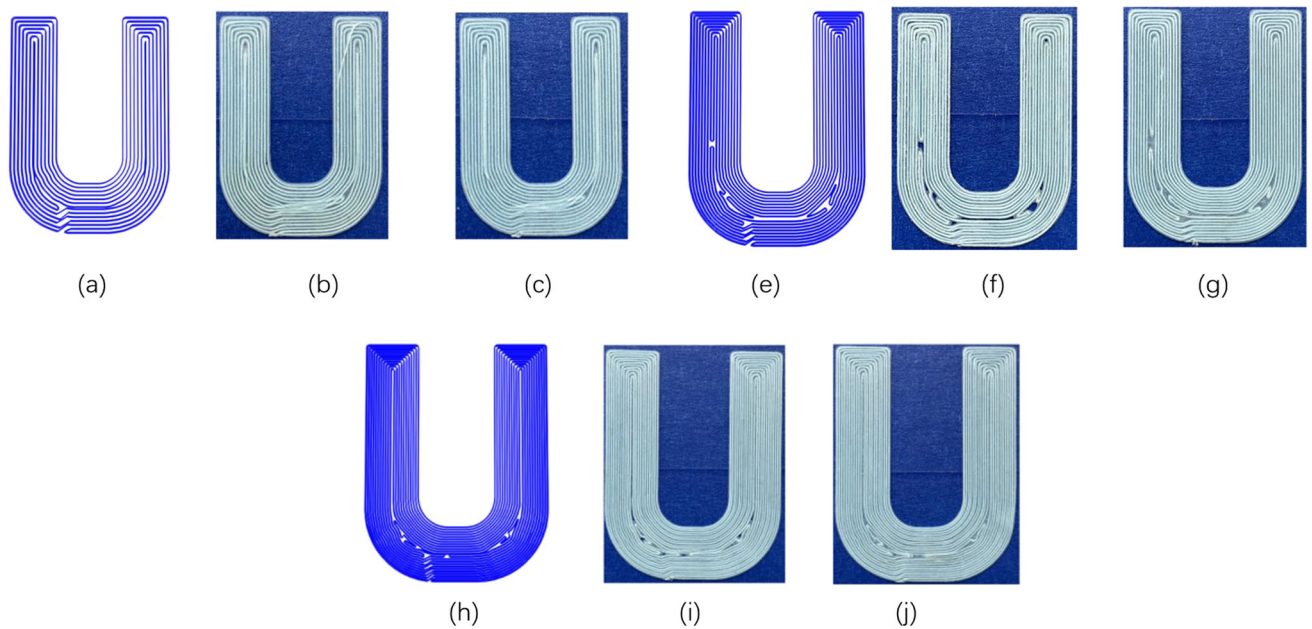


**Fig. 22** Experiment with different size samples of same shape. **a** Filling pattern of letter U (1x). **b** Print results before optimization. **c** Print results after optimization. **d** Filling pattern of letter U (1.2x). **e** Print

results before optimization. **f** Print results after optimization. **g** Filling pattern of letter U (1.5x). **h** Print results before optimization. **i** Print results after optimization

the optimization, the matrix extrusion increased and the fiber content decreased from 24.1 to 23.8%; however, the sample void ratio decreased by 45.7%, and the mechanical strength was still improved.

#### 6.4 Filling experiments

In order to verify the wider applicability of the CCO method, filling experiments were also conducted. The filling experiments are mainly divided into three groups: the first group is to explore the printing of the same sample model with different sizes, the second group is the printing of different models with more regular shapes, and the last group is the printing of different models with irregular shapes.

In the first group of experiments, the letter U with a length of 30 mm and a height of 40 mm was used as the basic sample. Using CFS filling with a deposition spacing of 0.6 mm, 0.7x, 1.2x, and 1.5x of the sample were printed (the first sample letter U in Sect. 4.3 was 0.7x, and the experimental figure was not repeated). As shown in Fig. 22, as the sample size increases, the filling paths become more and more dense, but the filling paths of the whole sample still have unstable deposition spacing. The paths of the basic sample letter U overlap, and there is no significant gap before and after optimization. It can be seen from Fig. 22f and h that in the 1.2x and 1.5x samples, the actual extruded amount of matrix does not satisfy the paths, resulting in a mismatch between the matrix

and fiber paths, and many holes exist in the samples. After optimization, the sample surface voids disappeared, and the print quality improved, as shown in Fig. 22g and j.

In the second set of experiments, the letters R, E, and M were printed. The letter R contained straight and curved paths, the letter E contained straight and smaller curved paths, and the letter M contained sharper paths. For the letter R, both CFS and Zigzag-filled specimens were printed, the former with a deposition spacing of 0.6 mm and the latter with 0.5 mm. For the letters E and M, both were Zigzag-filled with a deposition spacing of 0.65 mm and 0.6 mm, respectively. From Fig. 23, it can be seen that the CFS-filled samples are likely to have voids in the middle and the Zigzag-filled samples tend to have voids at the edges. Because there are more small corners in Zigzag filling, the fibers tend to deviate from the established path. However, regardless of the path and the given deposition spacing, the optimized amount of matrix extrusion results in more uniform sample filling and higher surface quality.

In the third set of experiments, four irregularly shaped samples were printed. Figure 24b shows the IICP sample under Zigzag filling, which is divided into regions according to stress distribution with a deposition spacing of 0.35 mm. Voids appear at the junction of each zone, and due to fiber rigidity and continuity, this porosity is increased or decreased during the printing process. Figure 24e shows a windmill sample under CFS filling with a deposition spacing of 0.6

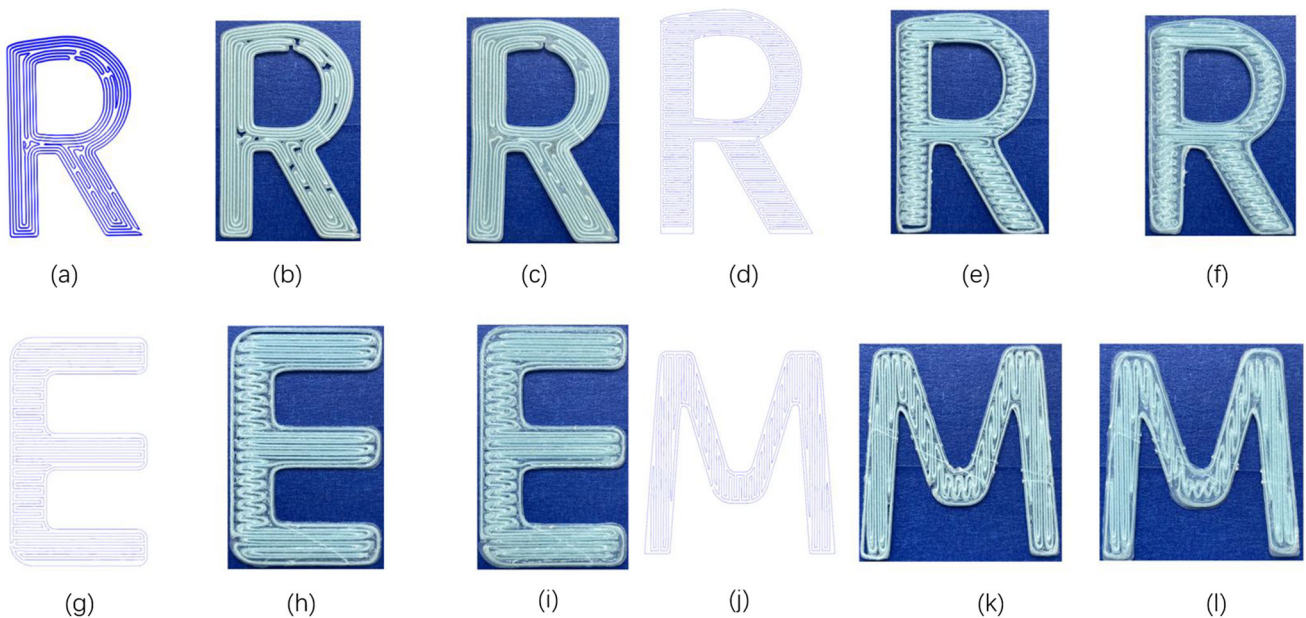


**Fig. 23** Experimentation on samples with regular geometry. **a** CFS filling pattern of R. **b** R(CFS) before optimization. **c** R(CFS) after optimization. **d** Zigzag filling pattern of R. **e** R (Zigzag) before optimization.

**f** R (Zigzag) after optimization. **g** Filling pattern of E. **h** E before optimization. **i** E after optimization. **j** Filling pattern of M. **k** M before optimization. **l** M after optimization

mm. Figures 24h and k illustrate a gear sample and a flower sample under Zigzag filling, both with a deposition spacing of 0.6 mm. There were more small curvature corners in the samples. This means that the fibers are more likely to deviate from the established path during printing, increasing the

difficulty of printing and the number of voids. After adaptive adjustment of the amount of matrix extrusion, the optimized samples not only filled the voids but also improved the matrix deflection problem caused by the fiber characteristics.

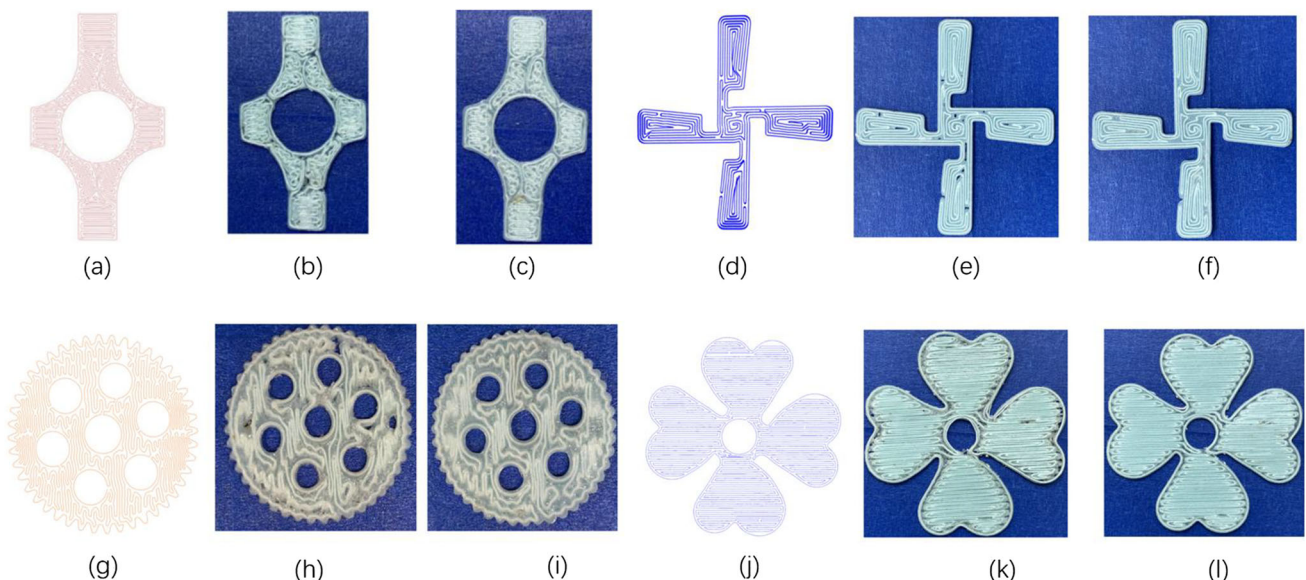


**Fig. 24** Experimentation on samples with irregular geometry. **a** Filling pattern of IICP. **b** IICP before optimization. **c** IICP after optimization. **d** Filling pattern of windmills. **e** Windmills before optimization.

**f** Windmills after optimization. **g** Filling pattern of gear. **h** Gear before optimization. **i** Gear after optimization. **j** Filling pattern of flower. **k** Flower before optimization. **l** Flower after optimization

## 7 Conclusion

This study proposes a CCO method based on a co-extrusion process. By analyzing the changes in the geometric sedimentation spacing in the path, an adaptive adjustment of the amount of matrix extrusion can be realized to improve the printing quality and strength. Through global smoothing and front-end processing of the amount of matrix extrusion, the matrix offset caused by the fiber characteristics was improved. Compared with the co-extrusion method without matrix adaptive adjustment, the tensile strength was increased by 18%, the bending strength was increased by 23.4%, and the porosity was reduced by 54.4%. The proposed method is applicable to any fiber-reinforced materials 3D printing part with a continuous path.

However, different fiber-reinforced materials have distinct physical properties, such as stiffness and interface, which can lead to the deformation of the deposition path. These path deformations are dynamic and cannot be estimated using fixed-path planning. To compensate for the amount of matrix extrusion more accurately, future work will combine data-driven and physical models. The degree of fiber deformation in the bending path will be estimated based on the physical properties of the fibers and process parameters.

**Author Contributions** Jinxiu Yang: designed the algorithms, experiments, and the drafted article. Yingxin Ma: provided continuous path filling method, experiments. Ling Chen: discussing, experiments designing and processing. Lijing Zhang: discussing, experiments designing and processing. Huanxiao Wu: completed part of the optimization algorithm. Yuan Yao: provided conceptualization, methodology, writing, review and editing.

**Funding** This work is partially supported by Nano-Science and Technology Research Center at Shanghai University and the Austrian Research Promotion Agency (the Natural 3D project 860384 grant).

**Availability of data and materials** Not applicable

## Declarations

**Ethics approval** Not applicable

**Consent to participate** Not applicable

**Consent for publication** Not applicable

**Conflict of interest** The authors declare no competing interests.

## References

- Reece LL, Fabrizio S, Valeska PT, Tr RS (2019) Multifunctional composites: a metamaterial perspective. *Multifunct Mater* 2(4):043001. <https://doi.org/10.1088/2399-7532/ab5242>
- Yaragatti N, Patnaik A (2021) A review on additive manufacturing of polymers composites. *Materials Today: Proceedings* 44(6):4150–4157. <https://doi.org/10.1016/j.matpr.2020.10.490>
- Struzziero G, Barbezat M, Skordos AA (2021) Consolidation of continuous fibre reinforced composites in additive processes: a review. *Additive Manufacturing* 48:102458. <https://doi.org/10.1016/j.addma.2021.102458>
- Justo J, Távara L, García-Guzmán L, París F (2018) Characterization of 3D printed long fibre reinforced composites. *Composite Structures* 185:537–548. <https://doi.org/10.1016/j.compstruct.2017.11.052>
- Araya-Calvo M, Lopez Gomez I, Chamberlain-Simon NK, León-Salazar JL, Guillén-Girón T, Corrales-Cordero JS, Sánchez-Brenes O (2018) Evaluation of compressive and flexural properties of continuous fiber fabrication additive manufacturing technology. *Additive Manufacturing* 22:157–164. <https://doi.org/10.1016/j.addma.2018.05.007>
- Cano-Vicent A, Tambuwala MM, Hassan SS, Barh D, Aljabali AAA, Birkett M, Arjunan A, Serrano-Aroca Á (2021) Fused deposition modelling: current status, methodology, applications and future prospects. *Addit Manuf* 47:102378. <https://doi.org/10.1016/j.addma.2021.102378>
- Oksman K, Skrifvars M, Selin J-F (2003) Natural fibres as reinforcement in polylactic acid (PLA) composites. *Compos Sci Technol* 63:1317–1324. <https://doi.org/10.1016/j.addma.2021.102378>
- Goh GD, Dikshit V, Nagalingam AP, Goh GL, Agarwala S, Sing SL, Wei J, Yeong WY (2018) Characterization of mechanical properties and fracture mode of additively manufactured carbon fiber and glass fiber reinforced thermoplastics. *Materials & Design* 137:79–89. <https://doi.org/10.1016/j.matdes.2017.10.021>
- Chen H, Wang J, Ni A, Ding A, Li S, Han X (2019) Effect of nano-OMMTs on mode I and mode II fracture toughness of continuous glass fibre reinforced polypropylene composites. *Composite Structures* 208:498–506. <https://doi.org/10.1016/j.compstruct.2018.10.003>
- Nakagawa Y, Mori K-i, Maeno T (2017) 3D printing of carbon fibre-reinforced plastic parts. *Int J Adv Manuf Technol* 91:2811–2817. <https://doi.org/10.1007/s00170-016-9891-7>
- Sharma P, Dhanopria AK, Joshi D (2020) An experimental study on carbon fiber thickness and layer thickness of depositing material in fused deposition modeling. *Materials Today: Proceedings* 44(6):4479–4484. <https://doi.org/10.1016/j.matpr.2020.10.722>
- Wang F, Wang G-T, Ning F, Zhang Z (2020) Fiber-matrix impregnation behavior during additive manufacturing of continuous carbon fiber reinforced polylactic acid composites. *Additive Manufacturing* 37:101661. <https://doi.org/10.1016/j.addma.2020.101661>
- Li H, Liu B, Ge L, Chen Y, Zheng H, Fang D (2021) Mechanical performances of continuous carbon fiber reinforced PLA composites printed in vacuum. *Composites Part B: Engineering* 225:109277. <https://doi.org/10.1016/j.compositesb.2021.109277>
- Agarwal K.M, Shubham P, Bhatia D, Sharma P, Vaid H, Vajpeyi R (2022) Analyzing the impact of print parameters on dimensional variation of ABS specimens printed using fused deposition modelling (FDM). *J Sens* 3:100149. <https://doi.org/10.1016/j.sintl.2021.100149>
- Parulski C, Jennotte O, Lechanteur A, Evrard B (2021) Challenges of fused deposition modeling 3d printing in pharmaceutical applications: where are we now? *Adv Drug Deliv Rev* 175:113810. <https://doi.org/10.1016/j.addr.2021.05.020>
- Goh GD, Yap YL, Agarwala S, Yeong WY (2019) Recent progress in additive manufacturing of fiber reinforced polymer composite. *Adv Mater Technol* 4(1):1800271. <https://doi.org/10.1002/admt.201800271>
- Yeong WY, Goh GD (2020) 3D printing of carbon fiber composite: the future of composite industry? *Mater* 2(6):1361–1363. <https://doi.org/10.1016/j.matt.2020.05.010>

18. Shi BH, Shang YY, Zhang P, Cuadros AP, Qu J, Sun BZ, Gu BH, Chou TW, Fu KK (2020) Dynamic capillary-driven additive manufacturing of continuous carbon fiber composite. *Matter* 2(6):1594–1604. <https://doi.org/10.1016/j.matt.2020.04.010>
19. Galetto M, Verna E, Genta G (2021) Effect of process parameters on parts quality and process efficiency of fused deposition modeling. *Comput Ind Eng* 156:107238. <https://doi.org/10.1016/j.cie.2021.107238>
20. Ćwikla G, Grabowik C, Kalinowski K, Paprocka I, Ociepka P (2017) The influence of printing parameters on selected mechanical properties of FDM/FFF 3D-printed parts. In: IOP Conference Series: Mater Sci Eng 227:012033. <https://doi.org/10.1088/1757-899X/227/1/012033>
21. Tian X, Tengfei L, Yang C, Wang Q, Li D (2016) Interface and performance of 3D printed continuous carbon fiber reinforced PLA composites. *Compos Part A Appl Sci Manuf* 88:198–205. <https://doi.org/10.1016/j.compositesa.2016.05.032>
22. Ueda M, Kishimoto S, Yamawaki M, Matsuzaki R, Todoroki A, Hirano Y, Duigou AL (2020) 3D compaction printing of a continuous carbon fiber reinforced thermoplastic. *Compos Part A Appl Sci Manuf* 137:105985. <https://doi.org/10.1016/j.compositesa.2020.105985>
23. Shuto R, Norimatsu S, Arola DD, Matsuzaki R (2022) Effect of the nozzle temperature on the microstructure and interlaminar strength in 3D printing of carbon fiber/polyphenylene sulfide composites. *Composites Part C: Open Access* 9:100328. <https://doi.org/10.1016/j.jcomc.2022.100328>
24. Zhao H, Chen B, Gu F, Huang QX, Garcia J, Yong C, Tu C, Benes B, Hao Z, Cohen-Or D (2016) Connected fermat spirals for layered fabrication. *ACM Trans Graph* 35(4):1–10. <https://doi.org/10.1145/2897824.2925958>
25. Zhang H, Yao Y, Ma Y, Lackner M, Jiang Y (2022) A 3D printing tool-path generation strategy based on the partition of principal stress field for fused filament fabrication. *Int J Adv Manuf Technol* 122(3–4):1719–1735. <https://doi.org/10.1007/s00170-022-09957-9>
26. Shaikh S, Kumar N, Jain PK, Tandon P (2016) Hilbert curve based toolpath for FDM process. In: CAD/CAM, Robotics and Factories of the Future: Proceedings of the 28th International Conference on CARs & FoF 2016, pp 751–759. [https://doi.org/10.1007/978-81-322-2740-3\\_72](https://doi.org/10.1007/978-81-322-2740-3_72)
27. Huang Y, Tian X, Wu L, Zia AA, Liu T, Li D (2023) Progressive concurrent topological optimization with variable fiber orientation and content for 3D printed continuous fiber reinforced polymer composites. *Composites Part B: Engineering* 255:110602. <https://doi.org/10.1016/j.compositesb.2023.110602>
28. Kubalak JR, Wicks AL, Williams CB (2019) Deposition path planning for material extrusion using specified orientation fields. *Proc Manuf* 34:754–763. <https://doi.org/10.1016/j.promfg.2019.06.209>  
47th SME North American Manufacturing Research Conference, NAMRC 47, Pennsylvania, USA
29. Zhang H, Chen J, Yang D (2021) Fibre misalignment and breakage in 3D printing of continuous carbon fibre reinforced thermoplastic composites. *Addit Manuf* 38:101775. <https://doi.org/10.1016/j.addma.2020.101775>
30. Hou Z, Tian X, Zhang J, Zheng Z, Zhe L, Li D, Malakhov AV, Polilov AN (2021) Optimization design and 3D printing of curvilinear fiber reinforced variable stiffness composites. *Compos Sci Technol* 201:108502. <https://doi.org/10.1016/j.compscitech.2020.108502>
31. Goh GD, Hamzah NMB, Yeong WY (2023) Anomaly detection in fused filament fabrication using machine learning. *3D Print Addit Manuf* 10(3):428–437. <https://doi.org/10.1089/3dp.2021.0231>

**Publisher's Note** Springer Nature remains neutral with regard to jurisdictional claims in published maps and institutional affiliations.

Springer Nature or its licensor (e.g. a society or other partner) holds exclusive rights to this article under a publishing agreement with the author(s) or other rightsholder(s); author self-archiving of the accepted manuscript version of this article is solely governed by the terms of such publishing agreement and applicable law.

## Authors and Affiliations

Jinxiu Yang<sup>1</sup>  · Yingxin Ma<sup>1</sup> · Ling Chen<sup>2</sup> · Lijing Zhang<sup>2</sup> · Huanxiao Wu<sup>1</sup> · Yuan Yao<sup>3,4</sup>

Jinxiu Yang  
2413940508@qq.com

Yingxin Ma  
3051998634@qq.com

Ling Chen  
maple.chen@cti-cert.com

Lijing Zhang  
zhanglijing@cti-cert.com

Huanxiao Wu  
2334535995@qq.com

<sup>1</sup> School of Mechatronic Engineering and Automation, Shanghai University, 99 Road Shanda, Shanghai 200444, China

<sup>2</sup> Centre Testing International (Shanghai) Co., 1996, XinJinqiao Road, Shanghai 201206, China

<sup>3</sup> Engineering Training Center, Shanghai University, 99 Road Shanda, Shanghai 200444, China

<sup>4</sup> Shanghai Key Laboratory of Intelligent Manufacturing and Robotics, Shanghai University, 99 Road Shanda, Shanghai 200444, China